energies

MDPI

Article

End Effect Equivalence in the 2-D Finite Element Analysis of a Line-Start Permanent Magnet Synchronous Motor with Hybrid Solid Rotor

Bo Yan, Xianglin Li *, Yue Sun and Yingjie Tan

College of Electrical Engineering, Qingdao University, Qingdao 266071, China; yb_qdu@qdu.edu.cn (B.Y.); 2021023765@qdu.edu.cn (Y.S.); tanyingjie95@126.com (Y.T.)
* Correspondence: lxllcc@126.com

Abstract: Reasonable end effect equivalence is of vital importance in the 2-D finite element analysis (FEA) for a line-start permanent magnet synchronous motor (LSPMSM) equipped with a hybrid solid rotor for improved starting and synchronous capabilities. In this work, a series of correction factors are applied to the rotor conductivity to include the end effect in the 2-D FEA model. Derivation of these correction factors completes after the separation of different torque components. A dynamic motor model of the LSPMSM is established with some parameters extracted from the 2-D FEA using the conductivity correction. Outcomes of this model exhibit good agreements with the 3-D FEA results, by which the introduced correction factors are validated to possess the acceptable precision and effectiveness.

Keywords: line-start permanent magnet synchronous motor (LSPMSM); hybrid solid rotor; rotor end effect; finite element analysis (FEA)

Citation: Yan, B.; Li, X.; Sun, Y.; Tan, Y. End Effect Equivalence in the 2-D Finite Element Analysis of a Line-Start Permanent Magnet Synchronous Motor with Hybrid Solid Rotor. *Energies* **2023**, *16*, 6766. https://doi.org/10.3390/en16196766

Academic Editor: Gianluca Brando

Received: 29 August 2023
Revised: 18 September 2023
Accepted: 20 September 2023
Published: 22 September 2023

1. Introduction

A line-start permanent magnet synchronous motor (LSPMSM) has a rotor involving both permanent magnets (PMs) and cage bars in the laminated core [1,2]. Such a hybrid rotor not only enables the LSPMSM to enjoy the outstanding steady-state performance such as high working efficiency and high power factor, but also provides the LSPMSM with a line-start capability [3]. Benefiting from these advantages, the LSPMSM has become a competent alternative to induction motors in many constant-speed applications with a long operation period (such as fans, compressors, and pumps) [4–6].

However, the LSPMSM usually performs quite poorly in terms of both starting and synchronization. The main reason is the braking torque caused by the mutual interaction between the stator-winding current and rotor PM flux [7]. During the starting process, the negative braking torque counteracts the positive induction torque and reduces the motor net torque. Consequently, the LSPMSM usually fails to synchronize or even fails to start up when the mechanical loads are relatively heavy [8,9].

Besides the defects resulting from the braking torque, the LSPMSM is also confronted with some challenges in the motor performance improvements. For instance, adding the cage resistance helps to increase the induction torque during the early starting stage but inevitably pulls down the same torque at the later starting stage [10]. On the other side, cutting down the PM sizes or contents helps to reach a lower level of braking torque while the motor steady-state properties are worsened at the same time [11,12].

To overcome the above-mentioned challenges, a hybrid solid rotor applied in the LSPMSM is designed and analyzed in [13–15] by the authors. Figure 1 shows the spatial views of the designed rotor. It can be seen that the conductive solid-steel blocks rather than the laminated steel sheets constitute the main rotor body. Selection of the solid steels is based on their inherent high starting torque [9,10]. A squirrel cage is attached to the steel

surface. The bars of the attached cage are divided into two groups, i.e., the trapezoidal ones with bigger areas (type I) and the rectangular ones with smaller areas (type II). When the motor is operating at the asynchronous stage, both the two types of cage bars provide the rotor with more eddy currents. As a consequence, the motor induction torque proportional to the rotor current density is lifted, and the motor starting and synchronization capabilities are improved.

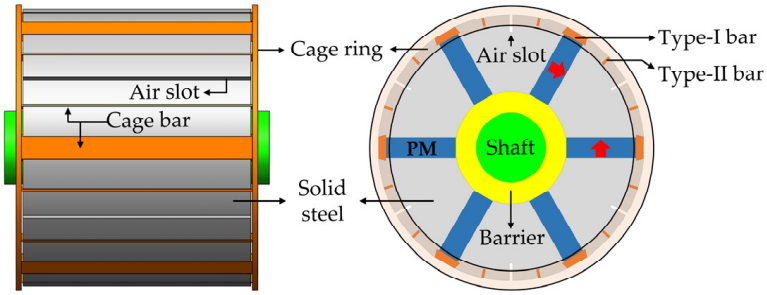

Figure 1. Spatial views of the hybrid solid rotor.

Apart from the added cage, some narrow air slots are also milled on the rotor periphery. When the rotation velocity is approaching the synchronous value, the milled slots force the rotor fluxes to penetrate deeper inside the rotor. Due to the inverse relationship between the flux penetration depth and the rotor slip, the rotation speed increases and the motor synchronization possibility is furtherly raised [16].

Performance evaluation of the LSPMSM with the hybrid solid rotor relies mainly on analyzing the transient motor behaviors under large amounts of operating conditions. The two-dimensional (2-D) time-stepping finite-element analysis (FEA) [17] is often selected to fulfill the extensive time-related analyses since it is able to rapidly and precisely predict the instantaneous motor outputs. It should be noted that rotor stack in the 2-D FEA model is assumed to possess an infinite axial length. Based on this assumption, the eddy currents induced in the rotor are treated as ones with only axial components. However, in practical 3-D cases, there exist two parts of non-axial currents flowing in different rotor segments. The first part is confined into the cage ring and can be taken into account in the 2-D FEA by an external cage circuit shown by Figure 2. In this circuit, the cage ring of either side is separated into two kinds of fractions. The first kind (ring fraction I) lies between the bars of type II while the second kind (ring fraction II) is sandwiched by the bars of types I and II. The two kinds of fractions are represented by their equivalent resistances and leakage inductances, respectively, i.e., $R_{\mathrm{end}}(\mathrm{I})/L_{\mathrm{end}}(\mathrm{I})$ for ring fraction I and $R_{\mathrm{end}}(\mathrm{II})/L_{\mathrm{end}}(\mathrm{II})$ for ring fraction II. The values of these resistances and inductances are measured by formulas in [18]. During the 2-D FEA, the type I and type II cage bars themselves are modelled as meshing elements and the current flowing inside the whole cage is calculated by inserting the electric–circuit equations into the 2-D FEA computation itself.

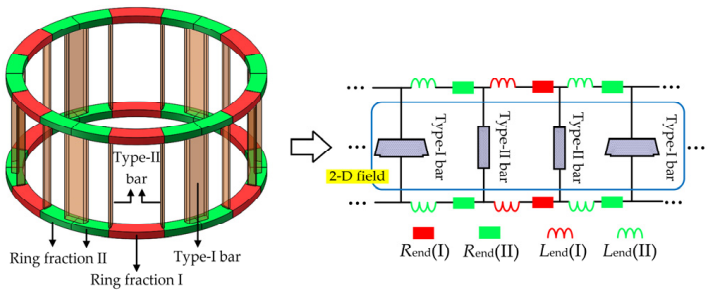

Figure 2. External circuit applied in the 2-D FEA to consider the cage ring currents.

The second part of non-axial rotor currents is constituted by those dwelling in the end regions of the solid steels. Figure 3 gives the distributions of axial eddy-current densities

with regard to two faces of the solid steel. Obviously, the axial densities have large values when they occur in the middle of steel but tend to be zero at the two ends of the steel. In other words, there flows a great deal of non-axial currents in the end regions of the solid steel. Unlike the first part of non-axial currents which are totally located in the cage ring, the second part existing in the steel end regions have no fixed circulating paths and hence cannot be measured in the 2-D FEA by the similar circuit introduction.

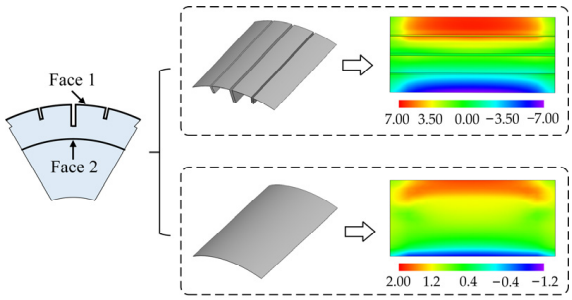

Figure 3. The axial current density distributions corresponding to two steel faces. Unit: 10^7 (A/m^{-2}).

Nevertheless, consideration of the effects of the non-axial currents in the steel end regions (also called end effects) can be fulfilled in the 2-D FEA by applying dimensionless factors to modify the actual steel conductivity. To date, numerous works of research associated with the correction factor solutions have been proposed. Some of them resorted to analytical algorithms in which idealized assumptions such as evenly distributed air-gap flux density [19], a rectangular magnetization curve [20], or turning the cylindrical rotor surface into a flat one [21] are required. Consequently, results dependent on these hypotheses do not reflect in detail the actual motor conditions and thus have doubtful accuracy when they are applied in the end effects measurement of the designed rotor. Other articles [22–25] obtained the correction factors by comparing the rotor losses computed by the 2-D and 3-D FEAs. Indeed, using the numeric methods is bound to achieve results with promising accuracies. However, all of these works of research are merely focused on the monolithic solid rotors without any attachments. For the hybrid solid rotor studied in this paper, the solid steels are separated by the PM poles and welded with a squirrel cage on their surface. To the authors' knowledge, few works concerned with the end effects of hybrid solid rotors have been carried out, and it is surprising that almost no attention has ever been paid to this research gap.

In this paper, the authors aimed to derive the correction factors merely concerning the solid steels, while the effects of the cage currents and PM fluxes on the solid steels are guaranteed at the same time. In this case, the correction factors are determined by two coherent steps. First, after the calculations of the 2-D and 3-D FEAs, the individual average induction torques merely caused by the solid steels defined by $T_{\omega\text{-2D}}$ and $T_{\omega\text{-3D}}$ are extracted from the total motor torques. Then, considering that the transient start-up of the studied LSPMSM can be approximated by the asynchronous steady-state operations under a series of different slips [16], the correction factors are confirmed by the principle that the extracted $T_{\omega\text{-2D}}$ and $T_{\omega\text{-3D}}$ are forced to equal with each other under the same rotor slips. Following this approximation, the torque equivalence in the time domain can be replaced by the counterpart in the slip domain, with which the calculation burden is reduced significantly.

This paper also validates the determined correction factors by three procedures. First, some motor parameters are calculated by the 2-D FEA with conductivity corrections on the rotor steels. Second, a dynamic motor model is established by coupling with the acquired parameters of the first step. Finally, the model transient outputs such as speed–time responses and torque–time curves are compared to those of the 3-D FEA, and the effectiveness of the proposed correction factors is testified by the good results agreement between the dynamic model and 3-D FEA.

The rest of this paper is organized as follows: Section 2 provides detailed descriptions about motor modeling in the *d*-*q* coordinate system and the following torque extraction. Section 3 states the procedure of confirming the correction factors. In Section 4, a series of motor parameters are first obtained by the 2-D FEA using conductivity corrections and then applied to establish a dynamic motor model. By comparing results of the dynamic model and 3-D FEA, the accuracies of the correction factors are validated. Section 5 draws the conclusion and gives the future research plans.

2. Motor Modeling and Torque Calculation

In this section, an analytical model of the LSPMSM with the hybrid solid rotor is established. With the given model, different motor torque components are calculated and separated with each other.

2.1. Model Description

Analysis on the transient behavior of the LSPMSM with the hybrid solid rotor can be realized by solving the system equations [3]. The magnets inserted into rotor core lead to the time variation in magnetic reluctance of per-phase stator winding [26,27]. Therefore, if the coordinate system is placed on the stator, the self and mutual inductances of the three-phase stator windings will change along with the rotor rotation, making it rather difficult to solve the system equations. To address this issue, the system equations are established on a rotating coordinate system in which one axis (*d*-axis) is in line with the central line of the permanent magnet flux and the other axis (*q*-axis) is ahead of the *d*-axis by 90 electrical degrees [28,29]. Both the *d*- and *q*-axes rotate in synchronization with the rotor. In this coordinate system as shown in Figure 4, the original three-phase stator windings are transformed into ones of ζ_{sq} and ζ_{sd}. The cage carrying eddy currents is equaled by the windings of ζ_{rcq} and ζ_{rcd}. Similarly, the conductive solid steels are replaced by the *q*- and *d*-axis windings as ζ_{rwq} and ζ_{rwd}. The PM poles are represented by their resultant flux ψ_{PM} which interacts with each of the *d*-axis windings but none of the *q*-axis ones. All the above-mentioned motor windings share the same rotation speed of N_r. The self-inductance of each *d*-axis winding or *q*-axis winding is almost invariant and the mutual inductance between two windings located at the *d*- and *q*-axes, respectively, is almost zero. These conditions reduce the complexity of the system equations and also the solution difficulty as a result.

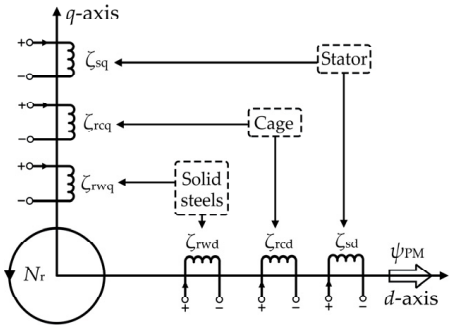

Figure 4. Motor winding distributions in the rotating coordinate system.

According to the winding arrangement of Figure 4, the flux linkage equations of the focused LSPMSM can be derived as

$$\begin{bmatrix} \psi_{sq} \\ \psi_{rcq} \\ \psi_{rwq} \\ \psi_{sd} \\ \psi_{rcd} \\ \psi_{rwd} \end{bmatrix} = \begin{bmatrix} L_{sq} & L_{mq} & L_{mq} & 0 & 0 & 0 \\ L_{mq} & L_{rcq} & L_{mq} & 0 & 0 & 0 \\ L_{mq} & L_{mq} & L_{rwq} & 0 & 0 & 0 \\ 0 & 0 & 0 & L_{sd} & L_{md} & L_{md} \\ 0 & 0 & 0 & L_{md} & L_{rcd} & L_{md} \\ 0 & 0 & 0 & L_{md} & L_{md} & L_{rwd} \end{bmatrix} \begin{bmatrix} i_{sq} \\ i_{rcq} \\ i_{rwq} \\ i_{sd} \\ i_{rcd} \\ i_{rwd} \end{bmatrix} + \begin{bmatrix} 0 \\ 0 \\ 0 \\ \psi_{PM} \\ \psi_{PM} \\ \psi_{PM} \end{bmatrix} \quad (1)$$

where $\psi_{sq}-\psi_{rcq}-\psi_{rwq}$, $i_{sq}-i_{rcq}-i_{rwq}$, and $L_{sq}-L_{rcq}-L_{rwq}$ are the flux linkages, currents, and self-inductances of $\zeta_{sq}-\zeta_{rcq}-\zeta_{rwq}$, $\psi_{sd}-\psi_{rcd}-\psi_{rwd}$, $i_{sd}-i_{rcd}-i_{rwd}$, $L_{sd}-L_{rcd}-L_{rwd}$ are the flux linkages, currents, and self-inductances of $\zeta_{sd}-\zeta_{rcd}-\zeta_{rwd}$, and L_{mq} and L_{md} are the q- and d-axis magnetizing inductances, respectively.

The motor voltage equations can be also obtained as

$$\begin{bmatrix} u_{sq} \\ 0 \\ 0 \\ u_{sd} \\ 0 \\ 0 \end{bmatrix} = \begin{bmatrix} R_s & & & & & \\ & R_{rcq} & & & & \\ & & R_{rwq} & & & \\ & & & R_s & & \\ & & & & R_{rcd} & \\ & & & & & R_{rwd} \end{bmatrix} \begin{bmatrix} i_{sq} \\ i_{rcq} \\ i_{rwq} \\ i_{sd} \\ i_{rcd} \\ i_{rwd} \end{bmatrix} + \frac{d}{dt} \begin{bmatrix} \psi_{sq} \\ \psi_{rcq} \\ \psi_{rwq} \\ \psi_{sd} \\ \psi_{rcd} \\ \psi_{rwd} \end{bmatrix} + \omega_r \begin{bmatrix} \psi_{sd} \\ 0 \\ 0 \\ -\psi_{sq} \\ 0 \\ 0 \end{bmatrix} \quad (2)$$

where u_{sq} and u_{sd} are the voltages applied to stator windings ζ_{sq} and ζ_{sd}, R_s is the stator winding resistance; $R_{rcq}/R_{rwq}/R_{rcd}/R_{rwd}$ are the winding resistances of $\zeta_{rcq}/\zeta_{rwq}/\zeta_{rcd}/\zeta_{rwd}$, and ω_r is the rotation angular frequency equaling $N_r 2\pi/60$, where P denotes the pole-pair number.

The motor torque equation is

$$T_e = \frac{3P}{2}\left(\psi_{sd} i_{sq} - \psi_{sq} i_{sd}\right) = T_R + T_{PM} + T_{cage} + T_{solid} \quad (3)$$

where

$$\begin{cases} T_R = \frac{3P}{2}\left(L_{sd} - L_{sq}\right) i_{sq} i_{sd} \\ T_{PM} = \frac{3P}{2}\psi_{PM} i_{sq} \\ T_{cage} = \frac{3P}{2}\left(L_{md} i_{rcd} i_{sq} - L_{mq} i_{rcq} i_{sd}\right) \end{cases} \quad (4)$$

and

$$T_{solid} = T_e - T_R - T_{PM} - T_{cage} \quad (5)$$

where T_R is the reluctance torque, T_{PM} the braking torque, T_{cage} the induction torque caused by the cage currents, and T_{solid} the induction torque generated by the solid steel currents.

2.2. Torque Component Calculation and Separation

It can be deduced from (4) and (5) that the solution of T_{solid} depends on the confirmations of quantities including (1) the total motor torque T_e, (2) the stator currents of i_{sq} and i_{sd}, (3) the inductances of $L_{sq}/L_{mq}/L_{sd}/L_{md}$, (4) the PM flux-linkage ψ_{PM}, and (5) the cage currents i_{rcq} and i_{rcd}. This paper utilizes the 2- and 3-D FEAs to calculate the five groups of motor quantities, after which the values of T_{solid} can be determined by the simple subtractions. Figure 5 displays the meshing views of the 2-D and 3-D FEA motor models.

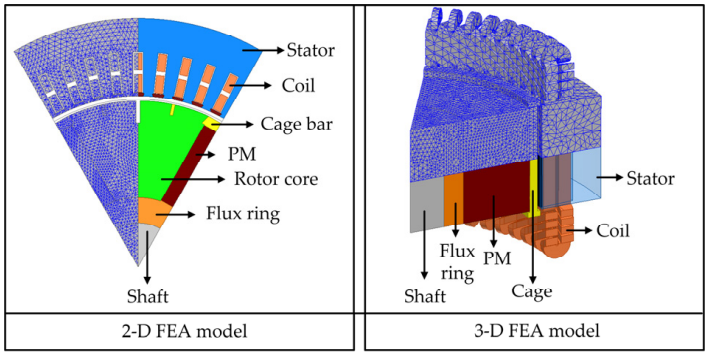

Figure 5. The 2- and 3-D FEA motor models with their respective meshing views.

To seek the balance between the solution accuracy and the computation cost, the maximum side length (MSL) of the triangular meshing elements in the 2-D FEA model is tentatively set to be 2, 4, or 6 mm, to which the number of meshing elements/connecting

nodes is 9320/7805, 6712/4729, or 5139/3765. As for the 3-D FEA model, the MSL of the pyramidal meshing elements is set to be 7, 10, or 13 mm, to which the number of meshing elements/connecting nodes is 17,608/12,515, 14,139/10,773, or 11,752/8061. Figure 6 shows the speed–time responses of the analyzed LSPMSM determined by the 2-D and 3-D FEA models with different meshing qualities. The load torque (named T_L) is set to be 3390 N. ·m and the combined inertia of rotor and load (named J_r) is set to be 10 kg·m^2. It can be found that the 2-D FEA model with MSL equal to 4 mm produces a speed–time response agreeing well with that predicted by the 2-D FEA model with MSL equal to 2 mm. Similarly, there exists a good agreement between results obtained by the 3-D FEA models of which the MSLs are 7 and 10 mm, respectively. Therefore, in this work, the MSL of the 2-D/3-D FEA model is set to be 4/10 mm to keep balance between the solution precision and rapidness.

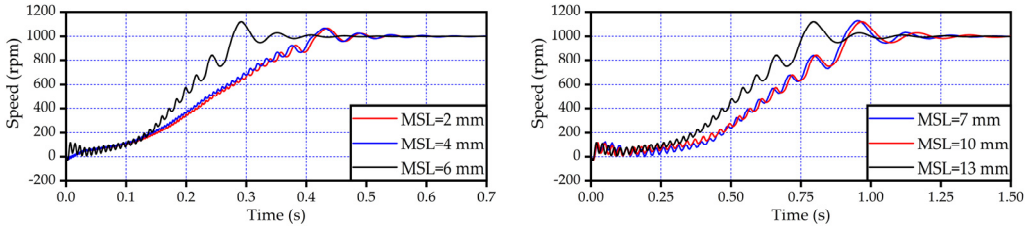

Figure 6. The speed–time responses obtained by the FEA models with different meshing qualities. (**a**) 2−D FEA model, (**b**) 3−D FEA model.

The process of calculating the five groups of motor parameters using the FEA models with meshing qualities discussed and defined as above is elaborated in the following context. For the sake of simplicity and readability, this paper only gives the calculation processes in the 2-D FEA, since they are kept unchanged in the 3-D FEA. The processes consist of four steps:

Step 1: A rotor slip sequence RS is defined as

$$\mathrm{RS} = \{s_i = 0.05i, i = 1, 2, \ldots, 20\} \tag{6}$$

and the rotor of the 2-D FEA model is sequentially forced to rotate at velocities corresponding to rotor slips of $s_i (i = 1, 2, \ldots, 20)$. Executing the 2-D FEA under each slip produces the steady-state values of electromagnetic torque as $T_e(s_i)$, stator-winding currents as $\boldsymbol{I}_s(s_i) = [i_A(s_i), i_B(s_i), i_C(s_i)]^T$, and stator-winding inductance matrix as

$$\boldsymbol{L}_s(s_i) = \begin{bmatrix} L_{AA}(s_i) & L_{AB}(s_i) & L_{AC}(s_i) \\ L_{AB}(s_i) & L_{BB}(s_i) & L_{BC}(s_i) \\ L_{AC}(s_i) & L_{BC}(s_i) & L_{CC}(s_i) \end{bmatrix} \tag{7}$$

where the diagonal elements are the self-inductances and the rest are the mutual inductances.

Applying the Park transformations to $\boldsymbol{I}_s(s_i)$ gives the q- and d-axis stator currents as

$$\begin{bmatrix} i_{sq}(s_i) & i_{sd}(s_i) \end{bmatrix}^T = \frac{2}{3}\boldsymbol{M}(s_i)\boldsymbol{I}_s(s_i) \tag{8}$$

where $\boldsymbol{M}(s_i)$ is the transformation matrix given as

$$\boldsymbol{M}(s_i) = \begin{bmatrix} -\sin\theta(s_i) & -\sin\left[\theta(s_i) - \frac{2}{3}\pi\right] & -\sin\left[\theta(s_i) + \frac{2}{3}\pi\right] \\ \cos\theta(s_i) & \cos\left[\theta(s_i) - \frac{2}{3}\pi\right] & \cos\left[\theta(s_i) + \frac{2}{3}\pi\right] \end{bmatrix} \tag{9}$$

where

$$\theta(s_i) = (1 - s_i)\omega_s t + \theta_0 \tag{10}$$

where ω_s is the synchronous angular frequency and θ_0 is the initial angle between phase A and d-axis.

Meanwhile, the q- and d-axis stator-winding self-inductances under each rotor slip can be determined as

$$\begin{bmatrix} L_{\mathrm{sq}}(s_i) & L_{\mathrm{sd}}(s_i) \end{bmatrix}^{\mathrm{T}} = \frac{2}{3}\boldsymbol{M}(s_i)\boldsymbol{L}_s(s_i)\boldsymbol{M}(s_i)^{\mathrm{T}} \tag{11}$$

and the q- and d-axis magnetizing inductances are confirmed as

$$\begin{bmatrix} L_{\mathrm{mq}}(s_i) & L_{\mathrm{md}}(s_i) \end{bmatrix}^{\mathrm{T}} = \begin{bmatrix} L_{\mathrm{sq}}(s_i) & L_{\mathrm{sd}}(s_i) \end{bmatrix}^{\mathrm{T}} - \begin{bmatrix} L_{\mathrm{ls}} & L_{\mathrm{ls}} \end{bmatrix}^{\mathrm{T}} \tag{12}$$

where L_{ls} is the leakage inductance of the stator windings.

Step 2: The currents flowing through cage bars (18 in total) under each rotor slip are obtained by integrating the current density across the bar area, i.e.,

$$i_{\mathrm{bar}}^{(k)}(s_i) = \iint_{A_k} J_k(s_i)\mathrm{d}s (k = 1, 2, \ldots, 18) \tag{13}$$

where A_{k} and $J_{\mathrm{k}}(s_{\mathrm{i}})$ are the total area and current density of the k-th bar conductor.

As displayed by Figure 7, the cage bars embedded in the rotor can be divided into three groups:

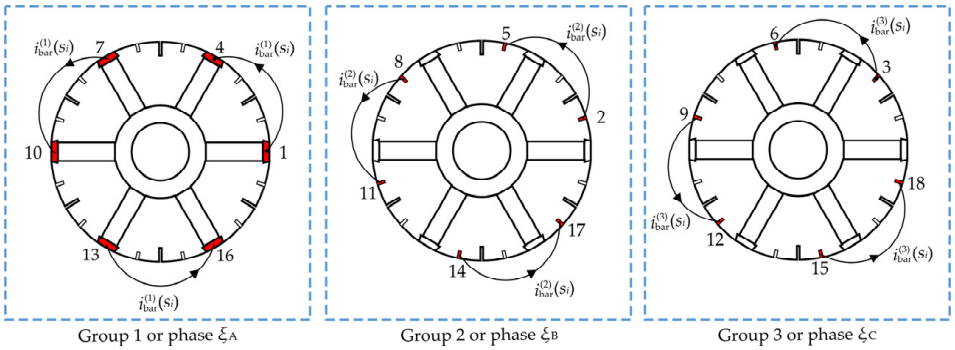

Figure 7. Bars group divisions and corresponding phase identifications.

The first group comprises the 1st, 4th, 7th, 10th, 13th, 16th bars, in which the flowing currents is $\pm i_{\mathrm{bar}}^{(1)}(s_i)$;

The second group covers the 2nd, 5th, 8th, 11th, 14th, 17th bars, in which the flowing currents is $\pm i_{\mathrm{bar}}^{(2)}(s_i)$;

The third group incorporates the 3rd, 6th, 9th, 12th, 15th, 18th bars, in which the flowing currents is $\pm i_{\mathrm{bar}}^{(3)}(s_i)$.

The three groups of cage bars can be identified as three cage phases ξ_{A}, ξ_{B}, and ξ_{C}, whose currents are $i_{\mathrm{bar}}^{(1)}(s_i)$, $i_{\mathrm{bar}}^{(2)}(s_i)$, and $i_{\mathrm{bar}}^{(3)}(s_i)$, respectively. With these phase identifications, the q- and d-axis cage currents under each rotor slip can be obtained as

$$\begin{bmatrix} i_{\mathrm{rcq}}(s_i) & i_{\mathrm{rcd}}(s_i) \end{bmatrix}^{\mathrm{T}} = \sqrt{2}\alpha_{\mathrm{sc}}\boldsymbol{M}_1{}^{-1}\begin{bmatrix} i_{\mathrm{bar}}^{(1)}(s_i) & i_{\mathrm{bar}}^{(2)}(s_i) & i_{\mathrm{bar}}^{(3)}(s_i) \end{bmatrix}^{\mathrm{T}} \tag{14}$$

where α_{sc} is the referring ratio given as

$$\alpha_{\mathrm{sc}} = (m_{\mathrm{r}}Q_{\mathrm{r}}K_{\mathrm{wc1}})/(m_{\mathrm{s}}Q_{\mathrm{s}}K_{\mathrm{ws1}}) \tag{15}$$

in which $m_{\mathrm{r}} = 3$ is the cage phase number, $m_{\mathrm{s}} = 3$ is the original stator phase number, $Q_{\mathrm{r}} = 3$ is the turns number per rotor phase, $Q_{\mathrm{s}} = 396$ is the turns number per stator phase, $K_{\mathrm{wc1}} = 1$ is the cage winding factor, $K_{\mathrm{ws1}} = 0.9452$ is the stator winding factor, and $\boldsymbol{M}_1$ is the inverse of the transformation matrix as

$$\boldsymbol{M}_1 = \begin{bmatrix} 0 & \sin\theta_1 & \sin(\theta_1+\theta_2) \\ 1 & \cos\theta_1 & -\cos(\theta_1+\theta_2) \end{bmatrix}^{\mathrm{T}} \tag{16}$$

where θ_1 is the angle difference between bar 1 and bar 2 and θ_2 is the angle difference between bar 2 and bar 3.

Step 3: For each slip, applying the frozen-permeability technique [30,31] to the 2-D FE model gives the stator-winding fluxes generated merely by the PM poles, i.e., $\psi_{\mathrm{A0}}(s_i)$, $\psi_{\mathrm{B0}}(s_i)$, and $\psi_{\mathrm{C0}}(s_i)$. The PM flux linkage under each rotor slip can then be determined as

$$\psi_{\mathrm{PM}}(s_i) = \frac{2}{3}\left[\cos\theta(s_i) \quad \cos\left[\theta(s_i)-\tfrac{2}{3}\pi\right] \quad \cos\left[\theta(s_i)+\tfrac{2}{3}\pi\right]\right]\left[\psi_{\mathrm{A0}}(s_i) \quad \psi_{\mathrm{B0}}(s_i) \quad \psi_{\mathrm{C0}}(s_i)\right]^{\mathrm{T}} \tag{17}$$

Step 4: By combining (8), (11), (12), (14), and (17) into (4), the reluctance torque, braking torque, the cage induction torque, and the solid-steel induction torque under each slip are confirmed, respectively, as

$$\begin{cases} T_{\mathrm{R}}(s_i) = \frac{3P}{2}\left[L_{\mathrm{sd}}(s_i) - L_{\mathrm{sq}}(s_i)\right] i_{\mathrm{sq}}(s_i) i_{\mathrm{sd}}(s_i) \\ T_{\mathrm{PM}}(s_i) = \frac{3P}{2}\psi_{\mathrm{PM}}(s_i) i_{\mathrm{sq}}(s_i) \\ T_{\mathrm{cage}}(s_i) = \frac{3P}{2}\left[L_{\mathrm{md}}(s_i) i_{\mathrm{rcd}}(s_i) i_{\mathrm{sq}}(s_i) - L_{\mathrm{mq}}(s_i) i_{\mathrm{rcq}}(s_i) i_{\mathrm{sd}}(s_i)\right] \\ T_{\mathrm{solid}}(s_i) = T_{\mathrm{e}}(s_i) - T_{\mathrm{R}}(s_i) - T_{\mathrm{PM}}(s_i) - T_{\mathrm{cage}}(s_i) \end{cases} \tag{18}$$

and the average value of $T_{\mathrm{solid}}(s_i)$ is obtained as

$$T_{w-2\mathrm{D}}(s_i) = \frac{1}{T}\int_{t_0}^{t_0+T} T_{\mathrm{solid}}(s_i)\mathrm{d}t \tag{19}$$

in which t_0 is the time point after which $T_{\mathrm{solid}}(s_i)$ becomes steady and T is the period of $T_{\mathrm{solid}}(s_i)$.

Repeating operations of step 1–4 in the 3-D FEA works out the average solid-steel induction torque under each slip, i.e., $T_{\omega\text{-}3\mathrm{D}}(s_i)$. The relationships of $T_{\omega\text{-}2\mathrm{D}}(s_i)$ and $T_{\omega\text{-}3\mathrm{D}}(s_i)$ versus slip are displayed in Figure 8. It can be seen that under each slip, the value of $T_{\omega\text{-}2\mathrm{D}}$ is bigger than that of $T_{\omega\text{-}3\mathrm{D}}$. The value gaps can be explained by the current–component differences of the 2-D and 3-D solid steels. In the 2-D solid steels, all the induced currents which comprise axial components and their flowing paths are as long as the rotor stack. Thus, all the steel currents contribute as the effective ones to generate the torque. However, in the 3-D solid steels, the non-axial currents in end regions push the axial ones into the middle portion of the steel body. As a result, the effective currents for torque production have flowing paths shorter than the rotor stack and hence lead to the torques turning smaller.

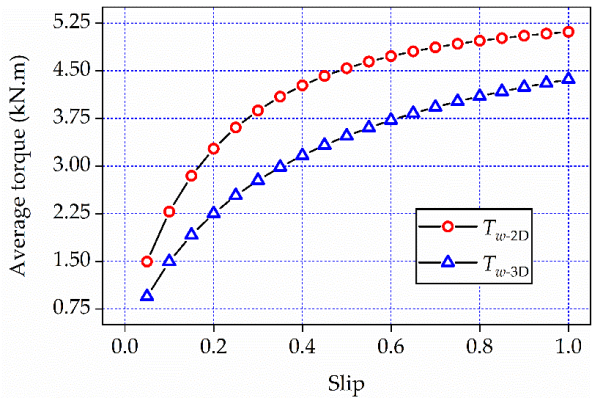

Figure 8. The curves of $T_{\omega\text{-}2\mathrm{D}}$ and $T_{\omega\text{-}3\mathrm{D}}$ versus slip.

3. Correction Factors Derivation

The torque differences shown by Figure 8 imply a conclusion that the end effects occurring in the 3-D solid steels can be considered and equaled in the 2-D solid steels, given that the value of $T_{\omega\text{-2D}}$ under each slip is modified to be equal to the value of $T_{\omega\text{-3D}}$. In this paper, the value equivalence between $T_{\omega\text{-2D}}$ and $T_{\omega\text{-3D}}$ is realized by applying the correction factors to the conductivity of 2-D solid steels. The following context states the detailed procedure for deriving these correction factors.

First, based on the given data of Figure 8 and the 4th-order polynomial fitting method, the functions of $T_{\omega\text{-2D}}$ and $T_{\omega\text{-3D}}$ versus slip can be obtained, respectively, as

$$\begin{cases} T_{w-2\text{D}} = f_{2\text{D}}(s) = 0.69 + 18.83s - 36.19s^2 + 33.9s^3 - 12.17s^4 \\ T_{w-3\text{D}} = f_{3\text{D}}(s) = 0.38 + 12.86s - 21.28s^2 + 19.34s^3 - 6.95s^4 \end{cases} \tag{20}$$

Considering the fact that the steel conductivity σ_c is a constant, the two above functions can be rewritten as

$$\begin{cases} T_{w-2\text{D}} = f'_{2\text{D}}(s\sigma_c) = & 0.69 + \left(18.83{\sigma_c}^{-1}\right)(s\sigma_c) - \left(36.19{\sigma_c}^{-2}\right)(s\sigma_c)^2 \\ & + \left(33.92{\sigma_c}^{-3}\right)(s\sigma_c)^3 - \left(12.17{\sigma_c}^{-4}\right)(s\sigma_c)^4 \\ T_{w-3\text{D}} = f'_{3\text{D}}(s\sigma_c) = & 0.38 + \left(12.86{\sigma_c}^{-1}\right)(s\sigma_c) - \left(21.28{\sigma_c}^{-2}\right)(s\sigma_c)^2 \\ & + \left(19.34{\sigma_c}^{-3}\right)(s\sigma_c)^3 - \left(6.95{\sigma_c}^{-4}\right)(s\sigma_c)^4 \end{cases} \tag{21}$$

Second, according to the functions given in Equation (21), the correction factor corresponding to each slip can be determined. For instance, the 3-D solid-steel induction torque under a certain slip s_u can be calculated by

$$T_{w-3\text{D}}(s_\text{u}) = f'_{3\text{D}}(s_\text{u}\sigma_\text{c}) \tag{22}$$

and its value is equivalent to modified 2-D induction torque under the same slip, i.e.,

$$f'_{2\text{D}}[s_\text{u}\sigma_\text{c}K_\text{ef}(s_\text{u})] = f'_{3\text{D}}(s_\text{u}\sigma_\text{c}) \tag{23}$$

where $K_\text{ef}(s_\text{u})$ is the conductivity correction factor under slip s_u. Based on (23), the expression of $K_\text{ef}(s_\text{u})$ can be confirmed as

$$K_\text{ef}(s_\text{u}) = \left(f'_{2\text{D}}\right)^{-1}\left[f'_{3\text{D}}(s_\text{u}\sigma_\text{c})\right]/(s_\text{u}\sigma_\text{c}) \tag{24}$$

Figure 9 shows the derived corrections factors with respect to the slip range. It can be seen that the factor values are in total smaller than one. Meanwhile, the phenomenon that the factors do not keep constant indicate that the end effects have different affecting levels when the slip varies.

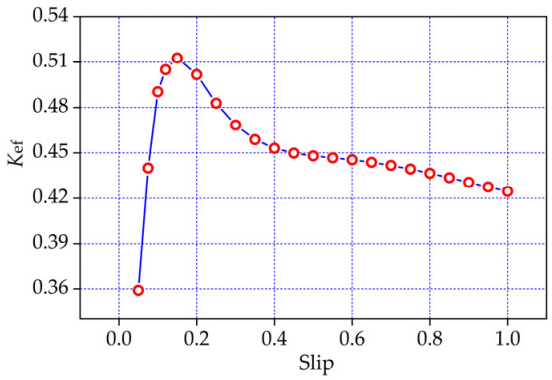

Figure 9. The curve of conductivity correction factors versus slip.

4. Correction Factors Validation

In this section, some vital parameters of the LSPMSM with the hybrid solid rotor are obtained by using the 2-D FEA, in which the solid steel conductivity is corrected with the factors given in Figure 9. The derived motor parameters pave a path for establishing a dynamic model of the focused LSPMSM. Both the steady-state and transient outputs generated by the dynamic model are in good agreement with those of the 3-D FEA, and the accuracies of the correction factors are hence testified by the acceptable result correlations.

4.1. Motor Parameters Calculation

This subsection presents below the detailed procedures for calculating the motor parameters by means of the 2-D FEA with solid-steel conductivity corrections.

First, a slip sequence is set as the same as RS given in (6). For each slip point s_i of the sequence RS, the 2-D solid-steel conductivity is defined as the original one σ_c times the corresponding correction factor $K_{ef}(s_i)$. Subsequently, the steady-state values of the stator-winding currents, flux linkages, and inductances under s_i are obtained, respectively, by the 2-D FEA as

$$\boldsymbol{I}'_s(s_i) = \begin{bmatrix} i'_A(s_i) & i'_B(s_i) & i'_C(s_i) \end{bmatrix}^T \tag{25}$$

$$\boldsymbol{\psi}'_s(s_i) = \begin{bmatrix} \psi'_A(s_i) & \psi'_B(s_i) & \psi'_C(s_i) \end{bmatrix}^T \tag{26}$$

and

$$\boldsymbol{L}'_s(s_i) = \begin{bmatrix} L'_{AA}(s_i) & L'_{AB}(s_i) & L'_{AC}(s_i) \\ L'_{AB}(s_i) & L'_{BB}(s_i) & L'_{BC}(s_i) \\ L'_{AC}(s_i) & L'_{BC}(s_i) & L'_{CC}(s_i) \end{bmatrix} \tag{27}$$

and the q- and d-axis stator-winding currents, flux linkages, self-inductances, and magnetizing inductances are determined, respectively, as:

$$\begin{bmatrix} i'_{sq}(s_i) & i'_{sd}(s_i) \end{bmatrix}^T = \frac{2}{3}\boldsymbol{M}(s_i)\boldsymbol{I}'_s(s_i) \tag{28}$$

$$\begin{bmatrix} \psi'_{sq}(s_i) & \psi'_{sd}(s_i) \end{bmatrix}^T = \frac{2}{3}\boldsymbol{M}(s_i)\boldsymbol{\psi}'_s(s_i) \tag{29}$$

$$\begin{bmatrix} L'_{sq}(s_i) & L'_{sd}(s_i) \end{bmatrix}^T = \frac{2}{3}\boldsymbol{M}(s_i)\boldsymbol{L}'_s(s_i)\boldsymbol{M}(s_i)^T \tag{30}$$

and

$$\begin{bmatrix} L'_{mq}(s_i) & L'_{md}(s_i) \end{bmatrix}^T = \begin{bmatrix} L'_{sq}(s_i) & L'_{sd}(s_i) \end{bmatrix}^T - \begin{bmatrix} L_{ls} & L_{ls} \end{bmatrix}^T \tag{31}$$

Second, based on the motor equivalent circuit [2] shown by Figure 10, the q- and d-axis rotor resistances $R_{rq}(s_i)/R_{rd}(s_i)$ and leakage inductances $L_{lrq}(s_i)/L_{lrd}$ (s_i) under slip s_i are obtained, respectively, as

$$\begin{cases} R_{rq}(s_i) = \text{Real}\left[\boldsymbol{E}'_{mq}(s_i)/\boldsymbol{I}'_{rq}(s_i) \right] R_{rd}(s_i) = \text{Real}\left[E'_{md}(s_i)/\boldsymbol{I}'_{rd}(s_i) \right] \\ L_{lrq}(s_i) = \frac{1}{s_i\omega_s}\text{Imag}\left[\boldsymbol{E}'_{mq}(s_i)/\boldsymbol{I}'_{rq}(s_i) \right] L_{lrd}(s_i) = \frac{1}{s_i\omega_s}\text{Imag}\left[\boldsymbol{E}'_{md}(s_i)/\boldsymbol{I}'_{rd}(s_i) \right] \end{cases} \tag{32}$$

where

$$\begin{cases} \boldsymbol{E}'_{mq}(s_i) = \boldsymbol{U}_{sq}(s_i) - [R_s + j(s_i\omega_s)L_{ls}]\boldsymbol{I}'_{sq}(s_i) - (1-s_i)\omega_s\boldsymbol{\psi}'_{sq}(s_i) \\ \boldsymbol{E}'_{md}(s_i) = \boldsymbol{U}_{sd}(s_i) - [R_s + j(s_i\omega_s)L_{ls}]\boldsymbol{I}'_{sd}(s_i) + (1-s_i)\omega_s\boldsymbol{\psi}'_{sq}(s_i) \end{cases} \tag{33}$$

and

$$\begin{cases} \boldsymbol{I}'_{rq}(s_i) = \boldsymbol{I}'_{sq}(s_i) - \boldsymbol{E}'_{mq}(s_i)/j(s_i\omega_s)L_{mq} \\ \boldsymbol{I}'_{rd}(s_i) = \boldsymbol{I}'_{sd}(s_i) - \boldsymbol{E}'_{md}(s_i)/j(s_i\omega_s)L_{md} \end{cases} \tag{34}$$

where $\boldsymbol{I}'_{sq}(s_i)/\boldsymbol{I}'_{sd}(s_i)$ are the complex amplitudes of $i'_{sq}(s_i)/i'_{sd}(s_i)$ and $\boldsymbol{U}_{sq}(s_i)/\boldsymbol{U}_{sd}(s_i)$ are the complex amplitudes of $u_{sq}(s_i)/u_{sd}(s_i)$ determined by ω_s.

$$\begin{bmatrix} u_{sq}(s_i) & u_{sd}(s_i) \end{bmatrix}^T = \frac{2}{3}\boldsymbol{M}(s_i)\begin{bmatrix} u_A & u_B & u_C \end{bmatrix}^T \tag{35}$$

where u_A, u_B, and u_C are the three-phase voltage sources.

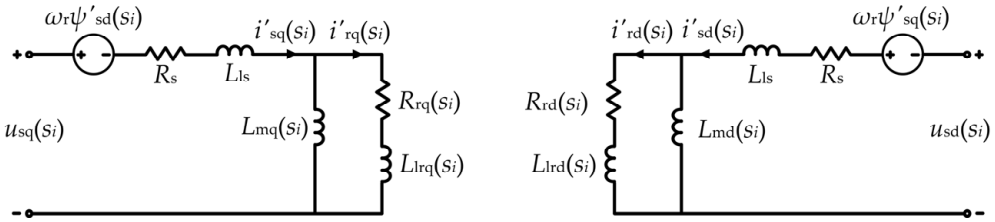

Figure 10. The motor equivalent circuit of the LSPMSM with the hybrid solid rotor.

Figure 11 shows the values of $R_{rq}(s_i)/R_{rd}(s_i)/L_{lrq}(s_i)/L_{lrd}(s_i)$ under the slip range RS. It can be seen that all these rotor parameters are not constant but exhibiting incremental or falling values when the rotor slip increases. The changing tendencies of these parameters can be explained by the eddy effects taking place in the conductive solid steels. When the rotor velocity changes, the area variance of the solid-steel eddy-current follows, and the rotor resistance and leakage inductances concerned with the current area are bound to possess the different values.

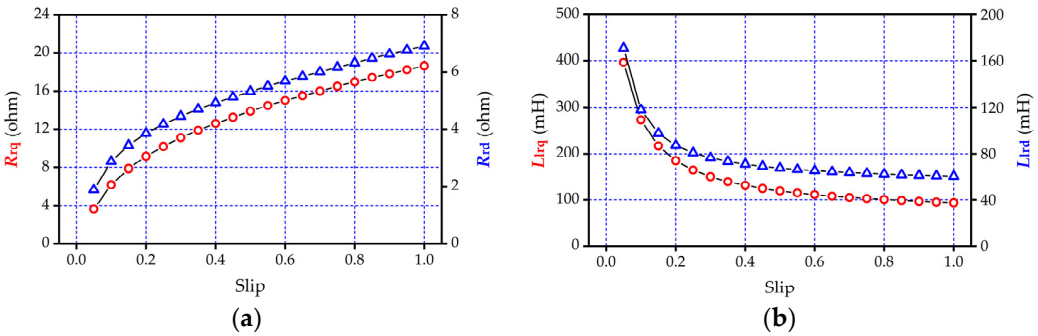

Figure 11. The rotor parameters calculated by 2-D FEA with solid-steel conductivity corrections. (**a**) rotor resistances, (**b**) rotor leakage inductances.

4.2. Dynamic Modeling and Result Comparisons

For the LSPMSM with the hybrid solid rotor, the mechanical rotation can be described as

$$T_e - T_L = J_r \frac{d\Omega_r}{dt} \tag{36}$$

where Ω_r is the angular speed of rotor (mechanical).

A dynamic model of the LSPMSM can be established by applying the inductances of (28), (29), and rotor parameters of Figure 10 into the flux-linkage Equation (1), voltage Equation (2), torque Equation (3), and rotation Equation (33). In this paper, a MATLAB/Simulink tool is utilized to realize the model foundation.

Figure 12 shows the model block distributions in the tool window. There are two loops in the model. The outer loop applies the time integral of the rotation speed, i.e., the rotor position, to the input of the *d*-*q* transformation block to obtain the *q*- and *d*-axis stator voltages. The inner loop works out the transient motor parameters by an interpolation block. Figure 13 shows the interior view of the interpolation block. In this block, the parameters determined in Section 4.1 are set as the known quantities. The parameters whose relevant slips are not covered by RS are calculated by the cubic-spline interpolation method.

The steady-state stator-winding currents and torques under slips of 0.2 and 0.8 are predicted by the dynamic model and compared to those of the 3-D FEA in Figure 14. The transient speed–time and torque–time responses under load conditions as 1 T_N-1 J_r and 1.2 T_N-3 J_r are calculated by the dynamic model and compared to those of the 3-D FEA in Figure 15. Taking the results of the 3-D FEA as the standard values, the mean relative errors (MREs) of the dynamic model outcomes are summarized in Table 1. Calculation of the MRE follows

$$\mathrm{MRE} = \frac{1}{N}\sum_{i=1}^{N}\left|\frac{y_{\mathrm{m}}^{i} - y_{\mathrm{3D}}^{i}}{y_{\mathrm{3D}}^{i}}\right| \tag{37}$$

where y_{m}^{i} and y_{3D}^{i} are the outcomes derived from the dynamic model and the 3-D FEA at the ith time point, respectively, and N is the total number of the time points.

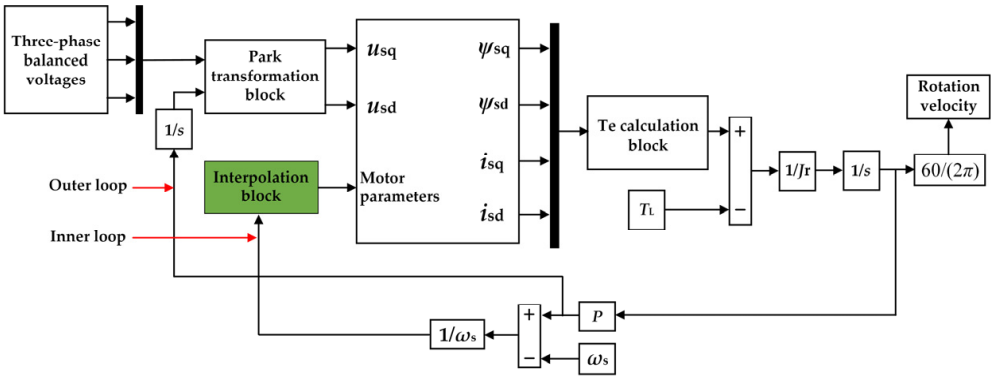

Figure 12. The established dynamic model of the LSPMSM with hybrid solid rotor.

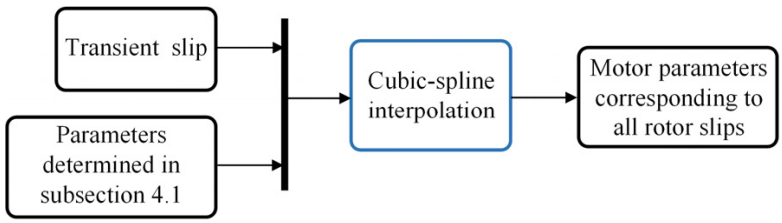

Figure 13. The interpolation block applied to derive the transient values of motor parameters.

Table 1. The MREs of the dynamic model results.

Figure Belongings	MRE (%)
Figure 14a,b	4.02 (i_{sq}) − 3.69 (i_{sd})/5.16 (i_{sq}) − 4.73 (i_{sd})
Figure 14c,d	6.19 (i_{sq}) − 4.62 (i_{sd})/3.52 (i_{sq}) − 4.15 (i_{sd})
Figure 14e,f	3.75/6.52
Figure 14g,h	3.18/4.79
Figure 15a,b	4.93/4.53
Figure 15c,d	4.74/4.36

It can be confirmed that both the good curve agreements shown by Figures 14 and 15 and the small errors displayed in Table 1 provide the sound accuracy validations for the dynamic model. Meanwhile, based on the fact that the model is established by the 2-D FEA using the solid-steel conductivity corrections, the given curve comparisons and errors exhibiting small values also testify the accuracies of the correction factors as well as the effectiveness of the paper-proposed method to consider the end effects in the 2-D FE motor model.

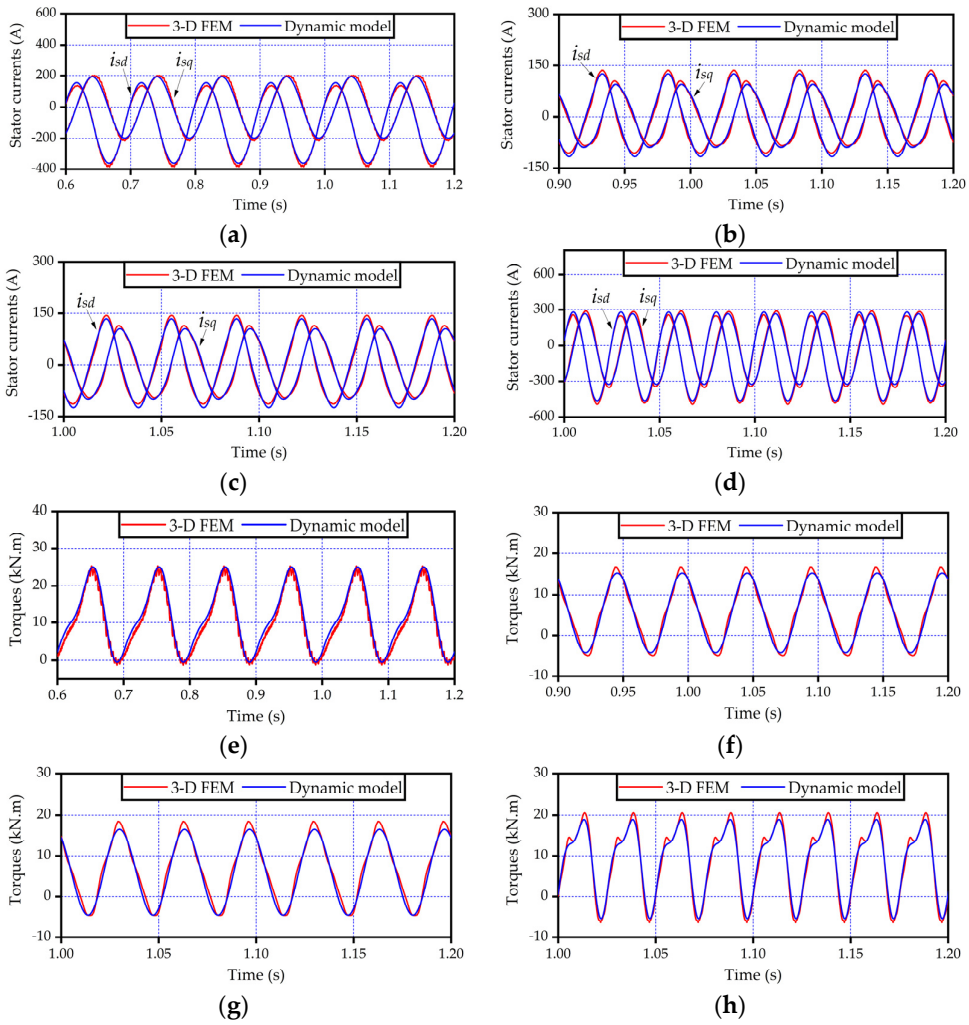

Figure 14. Comparisons of steady−state results including (**a**) stator currents under slip 0.2; (**b**) stator currents under slip 0.4; (**c**) stator currents under slip 0.6; (**d**) stator currents under slip 0.8; (**e**) torque under slip 0.2; (**f**) torque under slip 0.4; (**g**) torque under slip 0.6; (**h**) torque under slip 0.8.

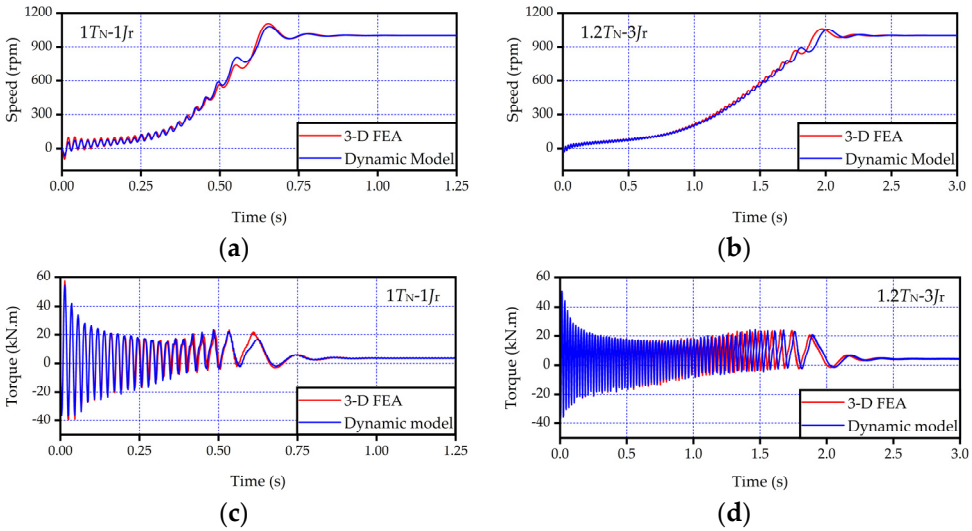

Figure 15. Comparisons of transient responses including (**a**) speed−time response under 1 T_N−1 J_r; (**b**) speed−time response under 1.2 T_N−3 J_r; (**c**) torque−time response under 1 T_N−1 J_r; (**d**) torque−time response under1.2 T_N−3 J_r.

5. Conclusions

Aimed at taking the end effect into consideration during the 2-D FEA of an LSPMSM with a hybrid solid rotor, this paper presented a method by which the solid-steel conductivity was modified with a series of correction factors. Derivation of these factors was based on the principle that the solid-steel induction torques predicted by the 2-D FEA were equal to those of the 3-D FEA. Motor parameters were determined by the 2-D FEA with conductivity correction. The acquired parameters were used to work out a dynamic model of the LSPMSM with the hybrid solid rotor. Both the steady-state and transient outcomes of the dynamic model achieved good result agreements with those of the 3-D FEA. The satisfying result correlations reflected the accuracies and effectiveness of the derived correction factors.

Nowadays, an LSPMSM with a hybrid solid rotor is under prototyping. In future research, the authors will put more efforts towards deeper investigations of end effect and further development of the conductivity correction method by the experimental results. Effects of two other critical factors including voltage level and temperature rise on the correction factor will be taken into account during further research. The correction factors applied to the conductivity under different voltage levels or temperature rises may be different, yet they can be also be determined via the equivalence between $T_{\omega\text{-2D}}$ and $T_{\omega\text{-3D}}$ under a series of rotation slips, by which the dynamic model involving the obtained factors is able to produce results with acceptable accuracy.

Author Contributions: Data curation, Y.S. and Y.T.; Writing—original draft, B.Y.; Writing—review & editing, X.L. All authors have read and agreed to the published version of the manuscript.

Funding: This research was supported in part by the Natural Science Foundation of Shandong Province under grant ZR2022QE247, in part by the Natural Science Foundation of Shandong Province under grant ZR2021YQ33, and in part by the National Natural Science Foundation of China under grant 51507191.

Data Availability Statement: No new data were created or analyzed in this study. Data sharing is not applicable to this article.

Conflicts of Interest: The authors declare no conflict of interest.

References

1. Marcic, T.; Stumberger, G.; Stumberger, B.; Hadziselimovic, M.; Virtic, P. Determining parameters of a line-start interior permanent magnet synchronous motor model by the differential evolution. *IEEE Trans. Magn.* **2008**, *44*, 4385–4388. [CrossRef]
2. Isfahani, A.H.; Vaez-Zadeh, S. Line start permanent magnet synchronous motors: Challenges and opportunities. *Energy* **2009**, *34*, 1755–1763. [CrossRef]
3. Palangar, M.F.; Soong, W.L.; Bianchi, N.; Wang, R.J. Design and optimization techniques in performance improvement of line-start permanent magnet synchronous motor: A review. *IEEE Trans. Magn.* **2021**, *57*, 900214. [CrossRef]
4. Mahmoudi, A.; Kahourzade, S.; Rahim, N.A.; Hew, W.P.; Uddin, M.N. Design, analysis, and prototyping of a novel-structured solid-rotor-ringed line-start axial-flux permanent-magnet motor. *IEEE Trans. Ind. Electron.* **2014**, *61*, 1722–1734. [CrossRef]
5. Isfahani, A.H.; Vaez-Zadeh, S. Effects of magnetizing inductance on start-up and synchronization of line-start permanent-magnet synchronous motors. *IEEE Trans. Magn.* **2011**, *47*, 823–829. [CrossRef]
6. Ding, T.; Takorabet, N.; Sargos, F.-M.; Wang, X. Design and analysis of different line-start PM synchronous motors for oil-pump applications. *IEEE Trans. Magn.* **2009**, *45*, 1816–1819. [CrossRef]
7. Ganesan, A.U.; Chokkalingam, L.N. Review on the evolution of technology advancements and applications of line-start synchronous machines. *IET Electr. Power Appl.* **2019**, *13*, 1–16. [CrossRef]
8. Fonseca, D.S.B.; Santos, C.M.C.; Cardoso, A.J.M. Stator faults modeling and diagnostics of line-start permanent magnet synchronous motors. *IEEE Trans. Ind. Appl.* **2020**, *56*, 2590–2599. [CrossRef]
9. Yan, B.; Wang, X.; Yang, Y. Comparative parameters investigation of composite solid rotor applied to line-start permanent-magnet synchronous motors. *IEEE Trans. Magn.* **2018**, *54*, 8206305. [CrossRef]
10. Yan, B.; Wang, X.; Yang, Y. Starting performance improvement of line-start permanent-magnet synchronous motor using composite solid rotor. *IEEE Trans. Magn.* **2018**, *54*, 7400504. [CrossRef]
11. Li, X.; Xue, Z.; Zhang, L.; Hua, W. A low-complexity three-vector-based model predictive torque control for SPMSM. *IEEE Trans. Power Electron.* **2021**, *36*, 13002–13012. [CrossRef]

12. Li, X.; Xue, Z.; Yan, X.; Zhang, L.; Ma, W.; Hua, W. Low-complexity multivector-based model predictive torque control for PMSM with voltage preselection. *IEEE Trans. Power Electron.* **2021**, *36*, 11726–11738. [CrossRef]
13. Yan, B.; Yang, Y.; Wang, X. Design of a large capacity line-start permanent magnet synchronous motor equipped with hybrid salient rotor. *IEEE Trans. Magn.* **2021**, *68*, 6662–6671. [CrossRef]
14. Yan, B.; Li, X.; Wang, X.; Yang, Y.; Chen, D. Magnetic field prediction for line-start permanent magnet synchronous motor via incorporating geometry approximation and finite difference method into subdomain model. *IEEE Trans. Ind. Electron.* **2023**, *70*, 2843–2854. [CrossRef]
15. Yan, B.; Li, X.; Wang, X.; Yang, Y.; Chen, D. An improved 2-D subdomain method towards electromagnetic-performance analysis of line-start permanent magnet synchronous motor. *IEEE Trans. Transport. Electrific.* **2023**, *9*, 4339–4351. [CrossRef]
16. Azari, M.N.; Mirsalim, M. Analytical modelling of a line-start permanent-magnet motor with slotted solid rotor. *IET Electr. Power Appl.* **2014**, *8*, 278–285. [CrossRef]
17. Ha, K.H.; Hong, J.P. Dynamic rotor eccentricity analysis by coupling electromagnetic and structural time stepping FEM. *IEEE Trans. Magn.* **2001**, *37*, 3452–3455. [CrossRef]
18. Chen, S. *Electric Machine Design*, 2nd ed.; China Machine Press: Beijing, China, 2004; pp. 383–385. ISBN 9787111020615.
19. Russel, R.L.; Norsworthy, K.H. Eddy currents and wall losses in screen-rotor induction motors. *Proc. IEE.* **1958**, *105*, 163–175. [CrossRef]
20. Angst, G. Polyphase induction motor with solid rotor; effects of saturation and finite length. *AIEE Trans.* **1962**, *80*, 902–909. [CrossRef]
21. Yee, H. Effects of finite length in solid-rotor induction machines. *Proc. IEE.* **1971**, *118*, 1025–1033. [CrossRef]
22. Ducreux, J.P.; Nicolas, G. Finite length effects study in massive iron rotors using 3D electromagnetic field computation. *IEEE Trans. Magn.* **1995**, *31*, 2096–2099. [CrossRef]
23. Jagiela, M.; Garbiec, T. Evaluation of rotor-end factors in solid-rotor induction motors. *IEEE Trans. Magn.* **2012**, *48*, 137–142. [CrossRef]
24. Papini, L.; Gerada, D.; Mebarki, A. High speed solid rotor induction machine: Analysis and performances. In Proceedings of the 17th International Conference on Electrical Machines and System (ICEMS 2014), Hangzhou, China, 22–25 October 2014. [CrossRef]
25. Garbiec, T. Fast computation of performance characteristics for solid-rotor induction motors with electrically inhomogeneous rotors. *IEEE Trans. Energy Convers.* **2016**, *31*, 1688–1696. [CrossRef]
26. Takahashi, A.; Kikuchi, S.; Miyata, K.; Binder, A. Asynchronous torque of line-starting permanent-magnet synchronous motors. *IEEE Trans. Energy Convers.* **2015**, *30*, 498–506. [CrossRef]
27. Marcic, T.; Stumberger, B.; Stumberger, G. Differential-evolution-based parameter identification of a line-start IPM synchronous motor. *IEEE Trans. Ind. Electron.* **2014**, *61*, 5921–5929. [CrossRef]
28. Pecho, J.; Hofmann, W. Analysis of start-up of line-start permanent magnet synchronous machines with anisotropic rotor reluctance. In Proceedings of the 2018 XIII International Conference on Electrical Machines (ICEM), Alexandroupoli, Greece, 3–6 September 2018.
29. Pecho, J.; Hofmann, W. Analytical approach and solution for line-start permanent magnet synchronous machines with anisotropic rotor reluctance. In Proceedings of the 2020 International Conference on Electrical Machines (ICEM), Gothenburg, Sweden, 23–26 August 2020.
30. Chu, W.Q.; Zhu, Z.Q. On-load cogging torque calculation in permanent magnet machines. *IEEE Trans. Magn.* **2013**, *49*, 2982–2989. [CrossRef]
31. Chu, W.Q.; Zhu, Z.Q. Average torque separation in permanent magnet synchronous machines using frozen permeability. *IEEE Trans. Magn.* **2013**, *49*, 1202–1210. [CrossRef]